AIAA JOURNAL
Vol. 42, No. 2, February 2004

Computational Methodology for Large-Eddy Simulation of Tip-Clearance Flows

Donghyun You*
Stanford University, Stanford, California 94305
Rajat Mittal†
George Washington University, Washington, D.C. 20052
and
Meng Wang‡ and Parviz Moin§
Stanford University, Stanford, California 94305

A large-eddy-simulation-based flow solver that combines an immersed-boundary technique with a curvilinear structured grid has been developed to study the temporal and spatial dynamics of an incompressible rotor-tip-clearance flow. The overall objective of these simulations is to determine the underlying mechanisms for low-pressure fluctuations downstream of the rotor near the end wall. Salient features of the numerical methodology, including the mesh topology, the immersed boundary method, the treatment of numerical instability for nondissipative schemes on highly skewed meshes, and the parallelization of the code for shared memory computer platforms, are discussed. The computational approach is shown to be capable of capturing the evolution of the highly complicated flowfield characterized by the interaction of distinct blade-associated vortical structures with the turbulent end-wall boundary layer. Simulation results are compared with experiments, and qualitative as well as quantitative agreement is observed.

Nomenclature

C	=	chord length
C_a	=	axial chord length
c	=	Smagorinsky coefficient
f_i	=	x_i component of body force
p	=	pressure
Re	=	Reynolds number
S_{ij}	=	strain rate tensor
Sr	=	Strouhal number
T	=	averaging timescale
t	=	time
U	=	time-averaged streamwise velocity
$U_{\max}$	=	time-averaged local maximum streamwise velocity
U_∞	=	inflow freestream velocity
u	=	streamwise velocity
u_i	=	x_i component of velocity
V_{belt}	=	moving end-wall velocity
v	=	cross-stream velocity
w	=	vertical velocity
x	=	streamwise coordinate
x_i	=	Cartesian coordinates
y	=	cross-stream coordinate
z	=	vertical coordinate
Δ	=	grid spacing
ρ	=	density
τ_{ij}	=	subgrid-scale stress tensor

Superscripts

-	=	filtered quantity
^	=	test-filtered quantity
+	=	quantity in wall-unit
′	=	fluctuation component

Received 2 June 2003; revision received 20 October 2003; accepted for publication 23 October 2003.

*Graduate Research Assistant, Department of Mechanical Engineering; dyou@stanford.edu. Student Member AIAA.

†Associate Professor, Department of Mechanical and Aerospace Engineering. Member AIAA.

‡Senior Research Scientist, Center for Turbulence Research, Stanford University/NASA Ames Research Center.

§The Franklin P. and Caroline M. Johnson Professor of Engineering, Department of Mechanical Engineering, and Director of Center for Turbulence Research, Stanford University/NASA Ames Research Center. Associate Fellow AIAA.

I. Introduction

THE existence of tip clearance between the rotor blade and casing wall is a major source of performance deterioration for axial turbomachines. In a transonic compressor, the interaction between the passage shock and the tip-leakage vortex is implicated in degradation of efficiency as well as noise generation.[1] Also, the tip clearance is responsible for a significant portion of performance losses in turbines, and the blade tip is known to be susceptible to damage from excessive thermal loading.[2] These issues have motivated a number of experimental and computational investigations of the tip-leakage flow configuration.[1–15]

For liquid handling systems like axial pumps and ducted propellers (Fig. 1), the rotor tip clearance is also considered to be the cause for low-pressure fluctuations downstream of the rotor in the vicinity of the end wall. Experimental studies of the incompressible rotor-tip-clearance flow[3–5] indicate that the low-pressure fluctuations can result from the turbulence associated with the tip-leakage vortex. Pressure measurements of Kang and Hirsch[6,7] show that the tip-leakage vortex dominates much of the end-wall flow region. The formation and size of the tip-leakage vortex is also known to be highly dependent on the size of the tip gap.[5] An incompressible compressor cascade studied by Storer and Cumpsty[8] with different tip-gap sizes showed that for smaller tip gaps (less than 1% of the chord) there was no clear indication of a tip-leakage vortex, whereas for tip gaps greater than 2% of the chord a tip-leakage vortex formed on the suction side of the blade.

Recently, Muthanna,[9,10] Wang,[11] and Kuhl[12] have made detailed measurements of the flowfield downstream of rotor blades in a low-speed linear compressor cascade employing stationary and moving end walls. One of the objectives in these studies was to

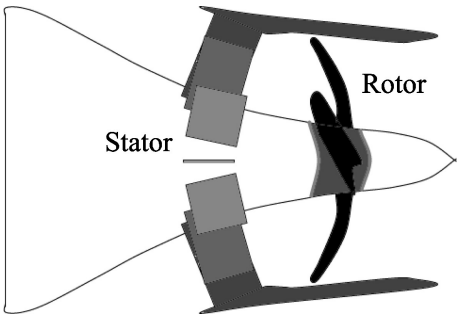

Fig. 1 Example of a ducted propeller with tip clearance.

examine the effect of the relative motion between the rotor blade tip and the casing on the tip-leakage flow. The results showed significant differences in the formation and the evolution of tip-leakage flows between the moving and stationary end-wall experiments. In the stationary end-wall case, Khorrami et al.[13] and Shin[14] have performed Reynolds-averaged Navier–Stokes (RANS) simulations and have shown reasonable predictions of mean velocity and pressure.

Although these and other experiments and numerical studies have provided useful information regarding the rotor-tip-clearance flow, significant gaps still exist in our knowledge of the dynamics of the tip-clearance flow as well as the resulting cavitation-inducing low-pressure fluctuations. This is primarily because of the difficulty in making detailed measurements in the vicinity of a moving blade or end-wall casing as well as in simultaneously measuring velocity, vorticity, and pressure. To understand the mechanisms for cavitation, it is necessary to study the detailed turbulence dynamics in the rotor-blade wake and the clearance region between the rotor tip and the endwall casing. Given the highly unsteady nature of the flow and the need to resolve a range of important flow structures, computational approaches based on the RANS equations are not ideally suited for a detailed analysis of this flow. In addition to this, time-accurate simulations of the tip-clearance configurations have been difficult because of the geometric complexity, which often leads to highly skewed, large-aspect-ratio meshes and very small computational time steps, and, therefore, have been tackled by a special mesh topology[1,2,13,15] or by an unstructured mesh approach.[14]

In the present study, we have used large-eddy simulation (LES) to simulate and study this flow. LES is especially suited for this type of flow because the Reynolds numbers, typically of $\mathcal{O}(10^5)$, are relatively low, which brings these flows within the reach of this modeling approach. Furthermore, LES provides detailed spatial and temporal information regarding a wide range of turbulence scales, which is precisely what is needed to gain better insight into the flow physics of this configuration.

The LES flow solver that has been developed for these simulations is fully three-dimensional with no statistically homogeneous directions and employs an immersed-boundary method in combination with a structured, curvilinear mesh topology to facilitate boundary condition application in the tip-gap region. This flow solver is used to simulate the experimental configuration of Wang[11] for a linear compressor cascade with a moving end wall. Despite the seeming simplicity of the chosen configuration, these are some of the most complex and ambitious large-eddy simulations attempted to date; each simulation requires a grid with $\mathcal{O}(10^7)$ points and $\mathcal{O}(10^5)$ time steps, which translate to $\mathcal{O}(10^5)$ single-processor CPU hours on SGI Origin 3800 per simulation. In addition, each simulation requires over 10GB of memory and over a Terabyte of disk space. Therefore, these simulations are feasible only on large-scale parallel computers. In this paper, we describe in detail the numerical and computational aspects of the LES flow solver developed for the tip-clearance flow, followed by a brief discussion of results from the simulation in comparison with the experimental measurements of Wang.[11] A more systematic analysis of the spatial-temporal dynamics of the flow and pressure fields and their implication to cavitation inception will be presented in a future publication.

II. Numerical Methodology

A. Numerical Method

The numerical method is based on the generalized-coordinate Navier–Stokes solver originally developed by Choi et al.,[16] with significant enhancements to treat the special difficulties associated with the tip-clearance flow. The spatially filtered Navier–Stokes equations for resolved scales in LES are as follows:

$$\frac{\partial \bar{u}_i}{\partial t} + \frac{\partial}{\partial x_j}\bar{u}_i\bar{u}_j = -\frac{\partial \bar{p}}{\partial x_i} + \frac{1}{Re}\frac{\partial}{\partial x_j}\frac{\partial \bar{u}_i}{\partial x_j} - \frac{\partial \tau_{ij}}{\partial x_j} \tag{1}$$

$$\frac{\partial \bar{u}_i}{\partial x_i} = 0 \tag{2}$$

where τ_{ij} is the subgrid-scale (SGS) stress tensor. All of the coordinate variables, velocity components, and pressure are nondimensionalized by the total chord C, the inflow freestream velocity U_∞, and ρU_∞^2, respectively. The time is normalized by C/U_∞. The governing equations (1) and (2) are rewritten in a conservative form in generalized coordinates. The dependent variables in the transformed Navier–Stokes equations are volume fluxes across the faces of the cells, which are equivalent to using the contravariant velocity components on a staggered grid multiplied by the Jacobian of the coordinate transformation. With this choice of variables, the discretized mass conservation can be easily satisfied. The terms in the transformed equations are described in detail in Ref. 16. The key feature of the numerical method is the use of a nondissipative, central-difference spatial discretization scheme, which has been demonstrated to be crucial for retaining the accuracy and predictive capability of the LES approach.[17,18]

The SGS stress tensor τ_{ij} is modeled by a Smagorinsky-type eddy-viscosity model:

$$\tau_{ij} - \tfrac{1}{3}\delta_{ij}\tau_{ij} = -2c\Delta^2|\bar{S}|\bar{S}_{ij} \tag{3}$$

Given that the tip-clearance flow is fully three-dimensional with no homogeneous directions, the Lagrangian dynamic SGS model[19] is employed in order to compute Smagorinsky coefficient c. The Lagrangian dynamic model averages the model coefficient along the flow-pathlines and therefore does not require a homogeneous direction.[20] The equation for computing the coefficient is

$$c^2(\boldsymbol{x}, t) = \Phi_{\mathrm{LM}}/\Phi_{\mathrm{MM}} \tag{4}$$

where

$$\Phi_{\mathrm{LM}} = \frac{1}{T}\int_{-\infty}^{t} L_{ij}M_{ij}[\boldsymbol{z}(t), t']e^{-(t-t')/T}\,\mathrm{d}t' \tag{5}$$

$$\Phi_{\mathrm{MM}} = \frac{1}{T}\int_{-\infty}^{t} M_{ij}M_{ij}[\boldsymbol{z}(t), t']e^{-(t-t')/T}\,\mathrm{d}t' \tag{6}$$

The identities L_{ij}, M_{ij}, and $\boldsymbol{z}$ are defined with velocity components u_i, grid spacing Δ, and strain-rate tensor S_{ij} as in the following:

$$L_{ij} = \widehat{\bar{u}_i\bar{u}_j} - \hat{\bar{u}}_i\hat{\bar{u}}_j \tag{7}$$

$$M_{ij} = 2\Delta^2(\widehat{|\bar{S}|\bar{S}_{ij}} - 4|\hat{\bar{S}}|\hat{\bar{S}}_{ij}) \tag{8}$$

$$\boldsymbol{z}(t') = \boldsymbol{x} - \int_{t'}^{t} \bar{\boldsymbol{u}}[\boldsymbol{z}(t''), t'']\,\mathrm{d}t'' \tag{9}$$

The integration method used to solve the transformed governing equations is based on a fully implicit fractional step method, which avoids the severe time-step restriction that would occur in the tip-clearance region. All terms including cross-derivative diffusion terms are advanced using the Crank–Nicolson method in time and are discretized by the second-order central difference in space. A Newton iterative method is used to solve the discretized nonlinear equations.

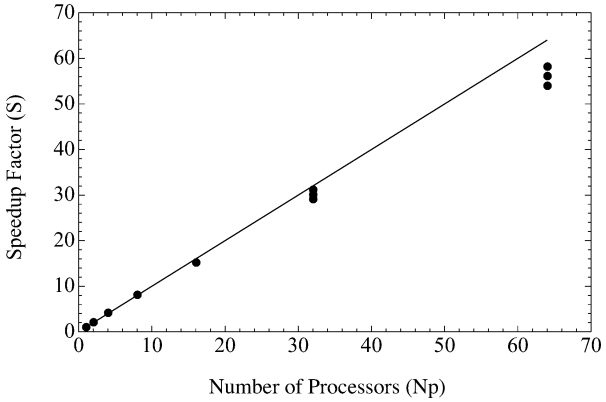

Fig. 2 Parallel performance of the solver on a SGI Origin 2000 platform: ——, linear speedup and ●, actual speedups obtained from three test runs at different times.

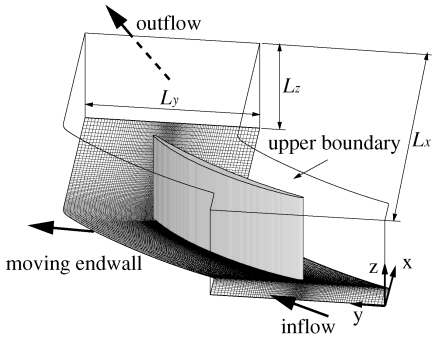

Fig. 3 Flow configuration and coordinate system for LES of rotor-tip-clearance flow.

Because the solution of the Poisson solver is the most expensive part of computation in this fully three-dimensional flow, it is crucial to employ a method that exhibits fast convergence as well as high parallel efficiency. In the current simulations, we employ a highly efficient multigrid procedure, which is also appropriate for parallelization. By experimenting with various solution methods, we have found that a combination of the line and red-black Gauss–Seidel multigrid method provides the most efficient solution procedure.

The entire code has been parallelized using multiprocessing directives (OpenMP) for shared memory platforms like SGI Origin 2000/3800 and Compaq GS320. Significant effort has been put into optimizing the parallel performance by utilizing cache-management strategies and minimizing data dependency. Figure 2 shows the speedup achieved for simulation of turbulent duct flow on a $256 \times 256 \times 256$ grid with up to 64 processors of SGI Origin 2000. The speedup factor S is defined by the ratio of the wall-clock time T_1 from a unit CPU to the wall-clock time T_N achieved using N-CPUs ($S = T_1/T_N$). Although comparable speedups have been observed in other shared memory platforms that have larger local memories, the present speedup might be biased by the inefficiency of nonuniform memory access when small number of processors are used. The solid line represents linear speedup, and symbols represent actual speedups obtained from the three different test runs at different times. The code achieves close to linear speedup thereby indicating nearly optimal parallel efficiency.

B. Flow Configuration

The flow configuration is schematically shown in Fig. 3 along with coordinate definition. The present study is focused on a linear cascade matching the experimental setup of Wang.[11] The rotor blade has a small tip clearance with the end wall, as shown in Fig. 4. The computational domain is of size $L_x \times L_y \times L_z = 1.6C \times 0.929C \times 0.5C$, where C is the chord length.

The full computational domain and grid distribution in a plane perpendicular to the blade (parallel to the end wall) are shown in Fig. 5a. The third direction is Cartesian with nonuniform grid

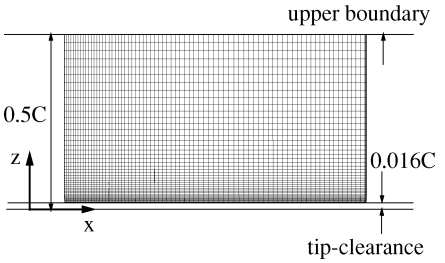

Fig. 4 Computational domain and Cartesian mesh distribution on the blade in the $x-z$ direction ($\frac{1}{2}$ lines plotted).

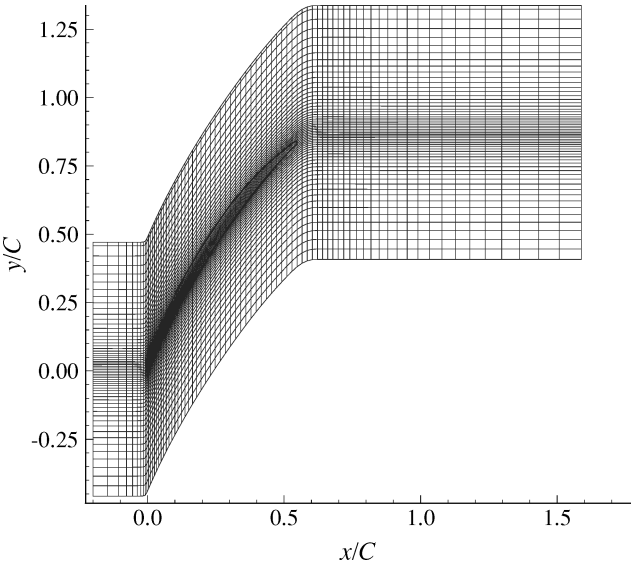

Fig. 5a Full computational domain and curvilinear mesh in the x–y plane used in conjunction with immersed boundary method for tip-clearance flow ($\frac{1}{6}$ lines plotted).

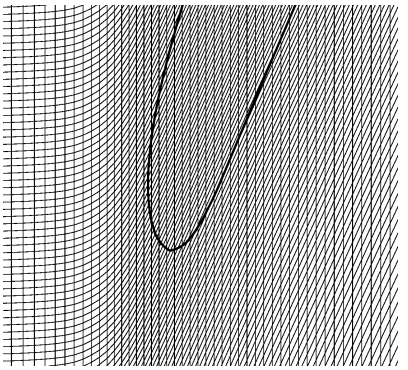

Fig. 5b Close-up view of the mesh near leading edge.

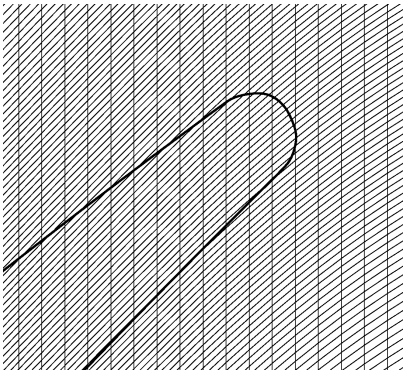

Fig. 5c Close-up view of the mesh near trailing edge.

distribution (Fig. 4). The rotor is placed near the inflow station so as to leave an adequate region for analysis of downstream turbulence. The simulation is performed in a frame of reference attached to the rotor, with a moving end wall mimicking the moving belt in the experiment.[11]

Periodic boundary conditions used along the y direction allow us to mimic the flow in the interior of the cascade. The y direction domain size $L_y = 0.929C$ as in the experiment. A simplification is made by terminating the blade span to one-half chord length and imposing inviscid flow boundary conditions on that boundary:

$$\frac{\partial u}{\partial z} = \frac{\partial v}{\partial z} = w = 0 \qquad \text{at} \qquad z = 0.5C \tag{10}$$

This is justified by observing that the root vortex at the hub does not play any significant role in the convected low-pressure fluctuations, which are found near the end walls. In Wang's experiment,[11] the tip-leakage vortex extends to about one-quarter of a chord length from the end wall. The inflow turbulent boundary-layer data are provided using the method of Lund et al.,[21] modified to account for the fact that the mean flow direction is not perpendicular to the inflow/outflow plane. No-slip boundary conditions are applied along the rotor blade and moving end wall:

$$u = w = 0, \qquad v = V_{\text{belt}} \qquad \text{at} \qquad z = 0 \tag{11}$$

and the convective boundary condition

$$\frac{\partial u_i}{\partial t} + U_c \frac{\partial u_i}{\partial x_1} = 0 \tag{12}$$

is applied at the exit boundary, where the convection speed U_c is set equal to the mean streamwise velocity integrated across the exit plane. The blade has a relatively high stagger angle of about 57 deg (see Fig. 5). This high stagger angle necessitates a highly skewed mesh and requires fine control of mesh parameters such as the grid stretching ratio and cell aspect ratio. The size of the tip clearance is 1.6% of the total chord, and the blade pitch is 0.9 chord. The Reynolds number of this flow is 4×10^5 based on the chord and inflow freestream velocity, and the inflow turbulent boundary layer has a Reynolds number of 780 based on the momentum thickness.

C. Mesh Topology and Immersed Boundary Method

The presence of the tip-clearance region between the rotor tip and the end wall poses a considerable challenge for the grid topology and resolution, and this factor has in fact been a major obstacle to the accurate prediction of this flow. Commonly used mesh topologies are the multizone mesh, which combines H- and O-type meshes (e.g., Refs. 1, 2, and 13), and the embedded H-type mesh (e.g., Ref. 15). However, the zonal mesh and the embedded H mesh have significant drawbacks for use in LES. This is so because the interpolation procedures in multizone meshes and the convergence of the longitudinal grid lines in the leading- and trailing-edge regions in embedded H-type meshes lead to high aspect and stretching ratios, which are inappropriate for nondissipative, energy-conservative numerical schemes.[18,22,23]

In recent years, the immersed boundary method[24] has emerged as a flexible and efficient tool for treating boundary conditions in complex geometries or even in moving geometries. With this approach, the simulations can be carried out on a simple grid (Figs. 5b and 5c for grid assignments near leading and trailing edges in tip-clearance configuration), and boundary conditions are assigned by applying body forces to the momentum equations to mimic the effect of the boundary:

$$f_i^n = \frac{\left(\bar{u}_{i(\text{desired})} - \bar{u}_i\right)^n}{\Delta t} + \frac{\partial}{\partial x_j}(\bar{u}_i \bar{u}_j)^n + \frac{\partial \bar{p}^n}{\partial x_i} - \frac{1}{Re}\frac{\partial}{\partial x_j}\frac{\partial \bar{u}_i^n}{\partial x_j} + \frac{\partial \tau_{ij}^n}{\partial x_j} \tag{13}$$

Figure 6 shows an example of body force assignment. Applying a linear or bilinear interpolation technique to point C of outside

Table 1 Comparison of the results from the present immersed boundary method with 321 × 321 mesh, body-fitted mesh simulation with 641 × 241 mesh,[25] and experiment[26]

Investigation	Re	C_D^{a}	$C_{L'}^{\text{b}}$	Sr
Present	60	1.40	0.134	0.136
	100	1.33	0.330	0.166
	160	1.31	0.560	0.188
Park et al.[25]	60	1.39	0.134	0.136
	100	1.33	0.320	0.165
	160	1.32	0.550	0.188
Williamson[26]	100	——	——	0.164

[a]Drag coefficient. [b]Lift coefficient.

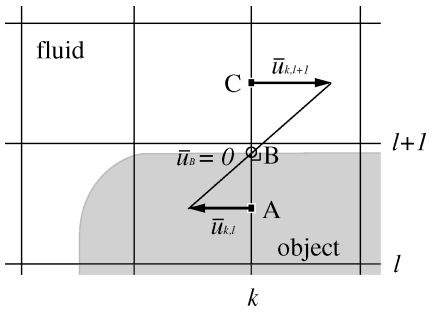

Fig. 6 Example of body forcing in the immersed boundary. A body force is assigned to point A using velocity $\bar{u}_{k,l}$, which is extrapolated from the velocities at B ($\bar{u}_B$) and C ($\bar{u}_{k,l+1}$).

velocity, $\bar{u}_{k,l+1}$, and to B of boundary velocity (e.g., zero in Fig. 6), the velocity inside of the boundary at A, $\bar{u}_{k,l}$ is estimated. Using this estimation and Eq. (13), the desired body force at the point is obtained.

The implementation of this immersed boundary method has been validated in a number of canonical flow problems. For example, Table 1 shows a comparison among the present simulation with immersed boundary method, simulation on body-fitted mesh,[25] and experiment[26] in the case of flow over a circular cylinder at low Reynolds numbers.

Although a Cartesian mesh is preferred because of the simplicity and efficiency of the solver, the need to resolve the thin turbulent boundary layers at high Reynolds numbers can lead to a very large mesh size if a Cartesian mesh is used. To overcome the preceding difficulty, a novel approach, which combines the immersed boundary technique with a structured grid in generalized curvilinear coordinates, is employed to treat the tip-gap region. The advantage of using a curvilinear mesh is that we can generate grid lines almost parallel to the blade surface, as demonstrated in Fig. 5. This ensures an adequate resolution of the boundary layers and allows periodic boundary conditions to be applied on the curved upper and lower boundaries. The immersed boundary method when used with the curvilinear mesh obviates a complex mesh topology and allows us to use a simple single-block mesh.

D. Grid Skewness and Numerical Stability

The large blade angle coupled with the need to have a periodic grid in the cross-stream direction leads to a mesh that is highly skewed over the blade surface. For such mesh topologies, nondissipative schemes, such as the one employed here, tend to exhibit highly enhanced dispersive error, which can affect the quality of computed results and sometimes even lead to numerical instability. This was our experience with preliminary simulation in this configuration as well as simulation of flow through a low-pressure turbine.[22,27]

It is well known that numerical instability for nondissipative schemes is often caused by the high local Peclet numbers, large mesh stretching ratio, large mesh aspect ratio, and mesh unsmoothness. Among these, the effect of mesh skewness is the least understood. In the current study, extensive tests have been carried out in order to examine various aspects related to grid skewness. A test

of various formulations of the nonlinear convection terms indicated that with a highly skewed mesh the divergence and skew-symmetric forms lead to superior stability characteristics as compared to the rotational form.[22]

In addition to this, truncation error analysis indicates that a central-difference discretization of the Navier–Stokes equations on a highly skewed and stretched mesh leads to spurious negative diffusion terms in the modified equation. However, a quantitative analysis using modified wave numbers shows that the increase of numerical errors is not significant up to quite a large skewness angle, which is larger than that present in the present study. Furthermore, it has been found that the mesh skewness does not alter the order of accuracy but does degrade the stability of explicit time-integration schemes. Thus, fully implicit time-integration methods are more appropriate for such grids. Further details regarding the analysis will be presented in a separate paper. Although grid skewness is controlled by the geometry of the blade, its negative effect can further be alleviated through careful control of the grid stretching ratio. In the current simulation, we therefore use meshes where the grid stretching ratio in both directions is kept small. This leads to an increase in the mesh size and consequently the computational resources.

Grid skewness related problems are usually not observed in conjunction with numerical schemes that employ numerical dissipation (either through upwinding, explicit addition of artificial dissipation, or through the use of stabilizers). However, unless carefully controlled, numerical dissipation can also overcome the SGS contribution, thereby reducing the accuracy and predictive capability of the LES approach. Furthermore, as shown by Gresho and Lee,[28] dissipative schemes do not provide any obvious warning of lack of resolution, whereas this is usually quite clear with nondissipative schemes because of the appearance of the so called "2-delta" waves. For these reasons, we strongly advocate the use of the nondissipative schemes for these types of computations despite the increase in computational resources that usually accompanies the use of these schemes.

III. LES of Tip-Clearance Flow

The newly developed solver is used to analyze the three-dimensional flow structures in the tip-clearance region and the dynamic interactions of the tip-leakage vortex with the end-wall turbulent boundary layer. The mesh size used for the present simulation is $449 \times 351 \times 129$ $(x \times y \times z)$. The grid spacings based on the chord in the streamwise, transverse, and spanwise directions are $9.9 \times 10^{-4} \le \Delta x/C \le 1.4 \times 10^{-2}$, $9.8 \times 10^{-4} \le \Delta y/C \le 6.5 \times 10^{-3}$, and $4.6 \times 10^{-4} \le \Delta z/C \le 1.2 \times 10^{-2}$, respectively. In wall units, the blade-surface resolution in the region of primary interest is within the range $\Delta x^+ \le 50$, $\Delta y^+ \le 3$, and $\Delta z^+ \le 30$. (Δz^+ increases up to 90 far from the tip-gap region.) A total of 36 mesh points are allocated across the tip-gap region, and this gives a normalized spanwise spacing of $\Delta z/C = 4.6 \times 10^{-4}$ or $0.3 \le \Delta z^+ \le 2.1$. The end-wall resolution in the tangential directions is $1.8 \le \Delta x^+ \le 95$ and $1.2 \le \Delta y^+ \le 100$. Prior to this simulation, coarser grid simulations had been carried out[22] to determine the resolution requirements, and the final fine mesh was subsequently constructed using this information. Because full investigation regarding grid resolution is virtually impossible with current computational resources available, simulations of a three-dimensional cascade without tip gap, which are less expensive than the present simulation, were performed with refined meshes in all three directions, and it was confirmed that results were relatively insensitive to the grid resolution. Figures 7 and 8 are examples of the study, which show reasonable robustness of the mean velocity u_1/U_∞, with respect to the grid resolution.

The simulation is advanced in time with maximum Courant–Friedrichs–Lewy (CFL) number equal to 4, which corresponds to $\Delta t U_\infty/C \approx 0.73 \times 10^{-3}$, and each time step requires a wall clock time of about 900 s when 32 CPUs of SGI Origin 3800 are used. The present results are obtained by integrating the governing equations over an interval of about $11C/U_\infty$.

In the experiments,[9–11] hot-wire measurements were made at four planes downstream of the blade trailing edge (two of which

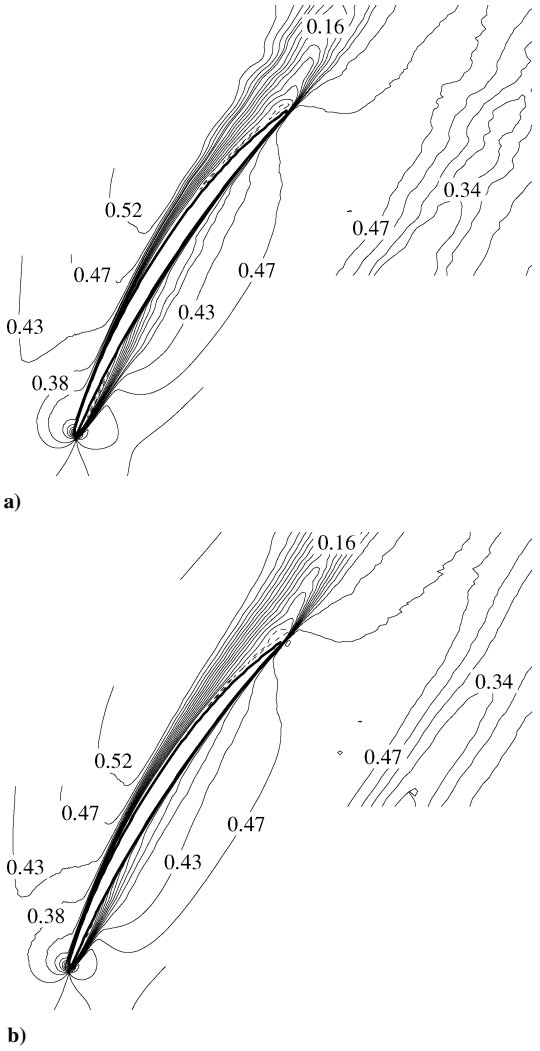

Fig. 7 Contour plots of mean velocity u_1/U_∞ in a linear cascade without tip gap: a) $449 \times 351 \times 8$ mesh ($\Delta z/C = 0.007$); and b) $897 \times 701 \times 16$ mesh ($\Delta z/C = 0.0035$). Contour levels are from -0.02 to 0.52 by 0.03, and negative values are dashed.

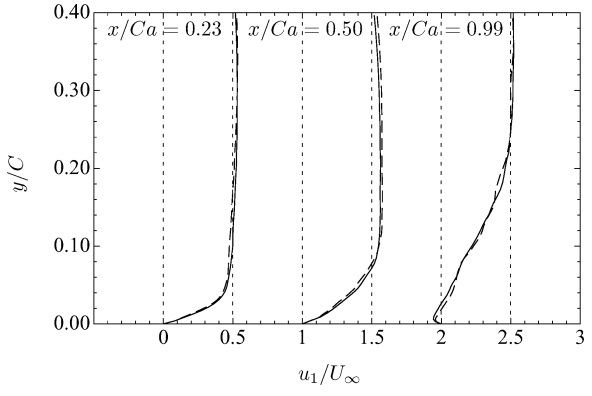

Fig. 8 Mean velocity u_1/U_∞ profiles on the suction surface: ——, $897 \times 701 \times 16$ mesh and - - - -, $449 \times 351 \times 8$ mesh.

are shown in Fig. 9) in order to quantify the mean and turbulence characteristics of the end-wall tip-leakage flow. To validate our LES computations, we have made qualitative as well as quantitative comparisons with the experimental data on these planes.

Figure 10 shows a visualization of an averaged flowfield using the λ_2-vortex technique of Jeong and Hussain.[29] The averaging time is $5C/U_\infty$, which gives us a reasonable view of the vortex topology associated with tip-leakage flow. The overall flow structures mainly consist of three distinct vortical regions. The vortical structures in A

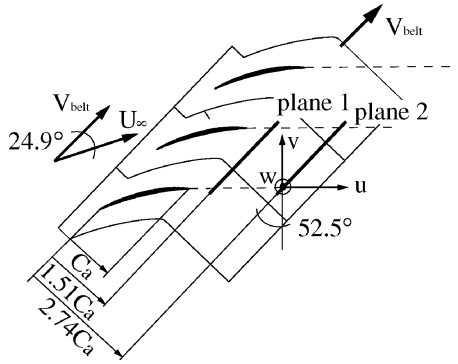

Fig. 9 Measurement planes where comparisons are made between present LES and experiment.[11]

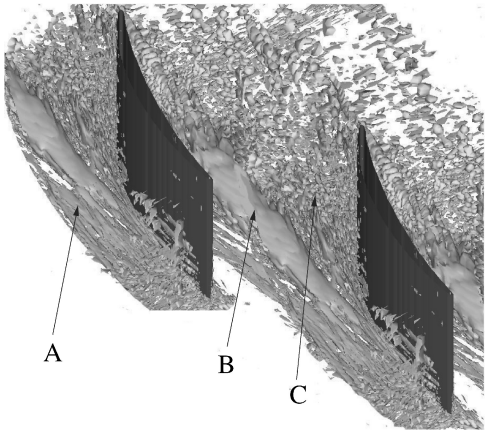

Fig. 10 The λ_2 isosurfaces from partially averaged flowfield: A, B, and C represent distinct vortical regions.

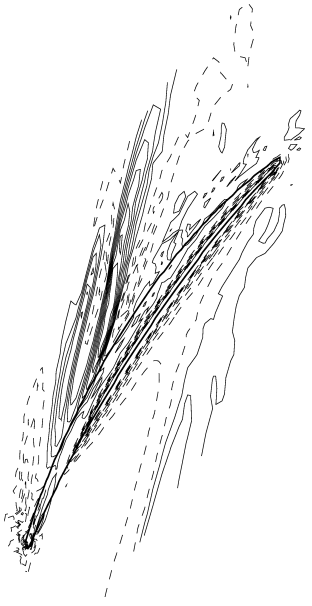

Fig. 11 Contour plot of mean spanwise velocity at $z/C_a = 0.0183$. 16 contour levels are plotted from −0.15 to 0.15, and negative values are dashed.

are generated near the leading edge and rotate in the direction opposite to the tip-leakage vortex in B. Small-scale vortical structures are abundant in the trailing-edge end-wall region C and are generated by the interaction between the tip-separation vortices and the tip-leakage vortex from the neighboring blade. Induced or passage vortical structures in region A of Fig. 10 along with tip-leakage vortex are more clearly observed in Fig. 11, where we plot the mean spanwise velocity contours in the x–y plane at $z/C_a = 0.0183$. Similar observations have been reported in experiments.[9–11] These complex vortical flows clearly affect the pressure distributions on both sides of rotor blade. As seen in Fig. 12, losses in pressure rise are noticeable near the end wall. The pressure distribution far from the end wall is generally comparable with that of experiment with stationary end wall[10] and indicates that the current mesh topology is capable of resolving the gross features of the flow. Marginal grid resolution on the blade boundary layer, especially near leading and trailing edges, might be responsible for the discrepancies observed in the pressure distribution in these regions.

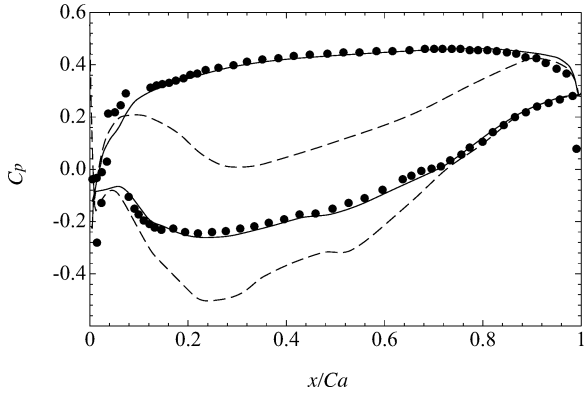

Fig. 12 Pressure distributions on the blade surface. Upper and lower lines and circles are from suction and pressure surfaces, respectively; ——, LES at $z/C_a = 0.916$; – – –, LES at $z/C_a = 0.03$; and ●, experiment[10] at $z/C_a = 0.916$.

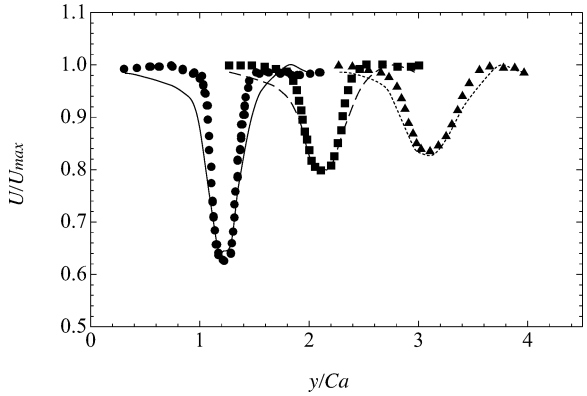

Fig. 13 Mean velocity profiles in the rotor-blade wake. Lines are from the present LES, and symbols are from the experiment[9]: ——, ●, $x/C_a = 1.366$; – – –, ■, $x/C_a = 2.062$; and . . . . , ▲, $x/C_a = 2.74$.

The wake profiles, which are obtained at $z/C_a = 1$ in the present LES and in the experiment with a stationary end wall,[9] are plotted in Fig. 13 in terms of the mean streamwise velocity. Here C_a is the axial chord length by which the locations are normalized. These wake profiles and the velocity contours in the subsequent figures are normalized by the local maximum velocity in the plane to account for any mass leakage in the experiments.[9–11,13] As seen in Fig. 13, the wake location is captured correctly by the LES in all of the measurement planes. The wider wake predicted by LES, which is also evident in Figs. 14–17, is most likely caused by the dispersive numerical errors inherent in the central-difference scheme. Discrepancies in velocity magnitudes, particularly on the pressure side, are also observed in the three downstream locations.

Figures 14 and 15 represent the streamwise velocity contours from the present LES and experiment[11] at $x/C_a = 1.51$ and 2.74, respectively, as seen by an observer looking upstream (see Fig. 9). Vertical bundles of the mean streamwise velocity contours are present in the wakes of rotor blades, and the tip-leakage vortices are found near the end wall in both the present LES and the experiment. Compared with the experimental findings, the tip-leakage vortex predicted by the LES is reasonable in size and location. An additional simulation configured with a double spanwise domain size (i.e., $L_z = C$) has also been carried out to investigate the domain size effect on the computed tip-leakage vortex. In Figs. 14a and 14b, we compare the

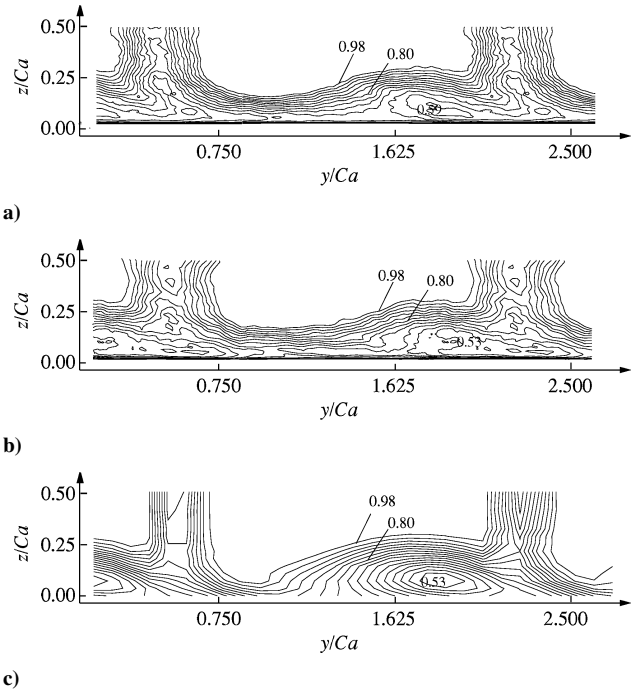

Fig. 14 Contour plots of mean streamwise velocity normalized by the local maximum velocity at $x/C_a = 1.51$: a) present LES, half-span; b) present LES, full span; and c) experiment.[11] Contour levels are from 0.5 to 0.98 by 0.03.

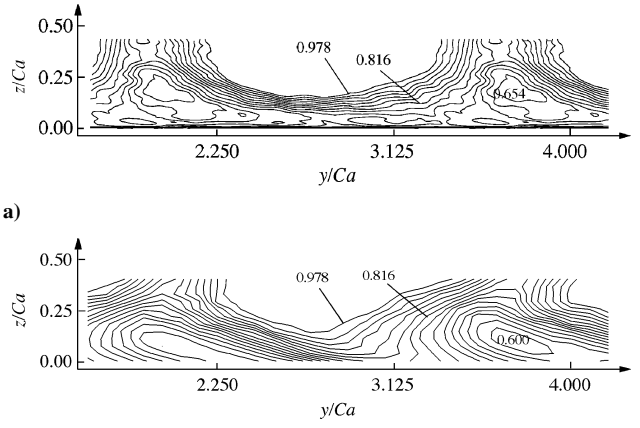

Fig. 15 Contour plots of mean streamwise velocity normalized by the local maximum velocity at $x/C_a = 2.74$: a) present LES and b) experiment.[11] Contour levels are from 0.6 to 0.978 by 0.027.

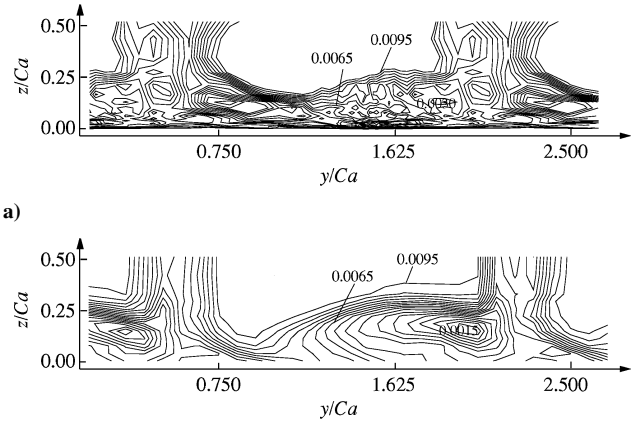

Fig. 16 Contour plots of $\overline{u'u'}$ at $x/C_a = 1.51$: a) present LES and b) experiment.[11] Contour levels are from 0.001 to 0.0095 by 0.0005.

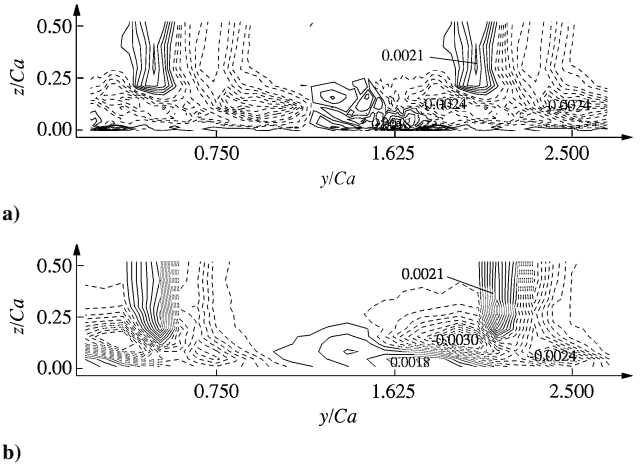

Fig. 17 Contour plots of $\overline{u'v'}$ at $x/C_a = 1.51$: a) present LES and b) experiment.[11] Contour levels are from −0.003 to 0.003 by 0.0003, and negative values are dashed.

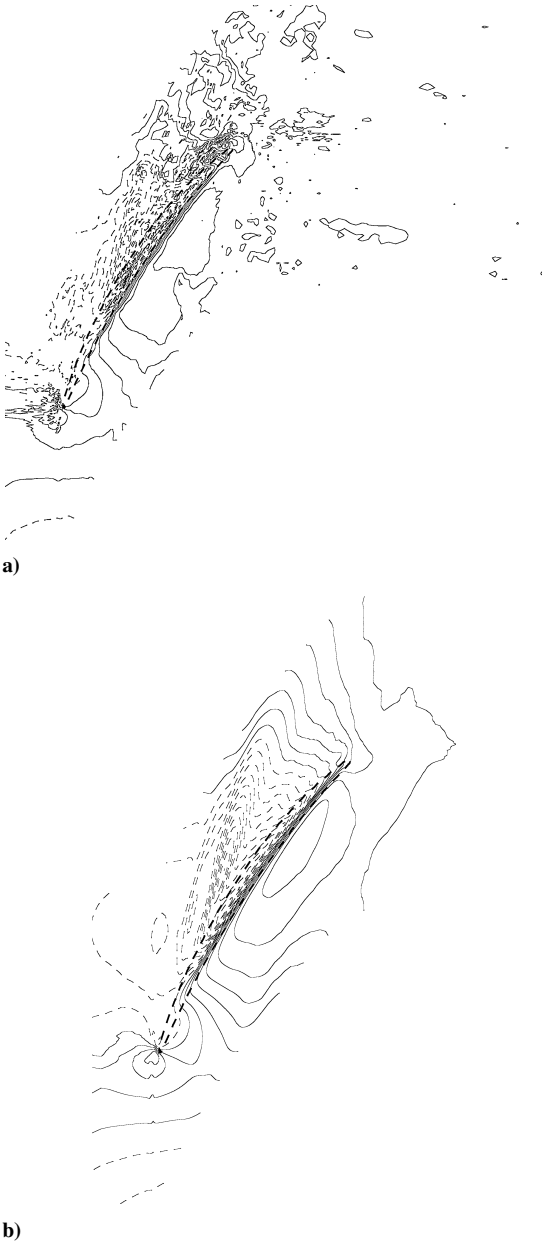

Fig. 18 Pressure contours in the tip-gap region ($z/C_a = 0.008$): a) instantaneous and b) time-averaged. Contour levels are from −0.35 to 0.18 by 0.03, and negative values are dashed.

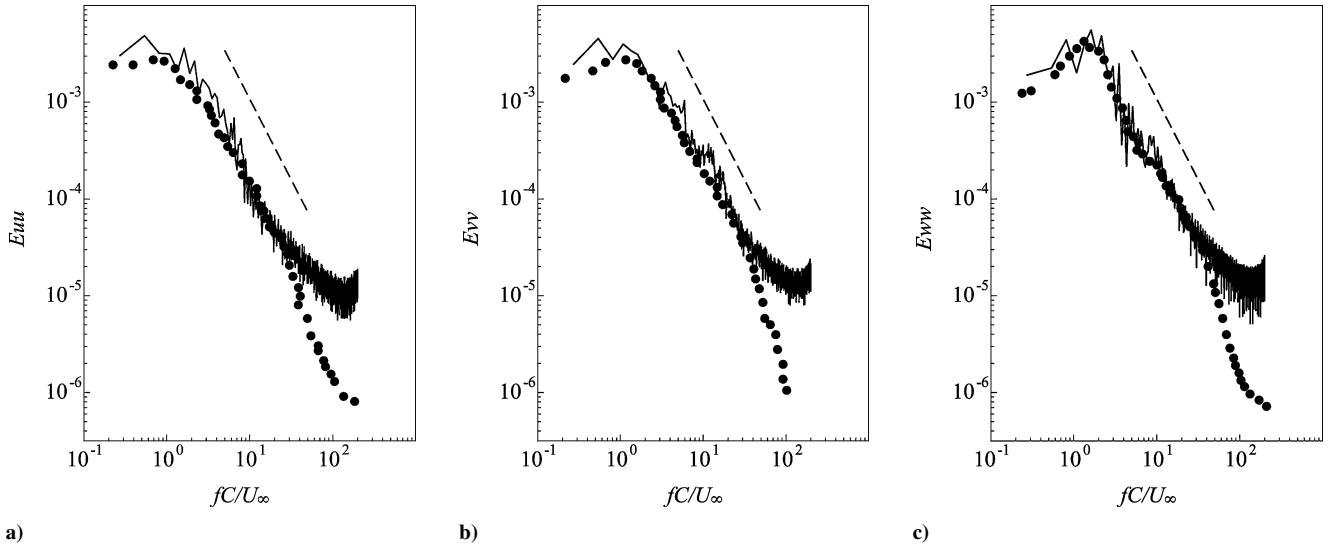

Fig. 19 Energy spectra as a function of frequency in the tip-leakage region at $x/C_a = 1.51$, $y/C_a = 1.4$, and $z/C_a = 0.1$: a) E_{uu}, b) E_{vv}, and c) E_{ww}, with ——, LES; ● , experiment[11]; and – – –, $-\frac{5}{3}$ slope.

computed tip-leakage vortex at the downstream plane for these two simulations and note that the difference are quite minimal. Thus, in contrast to Shin's RANS study of a stationary end-wall case,[14] which generates a stronger and bigger tip-leakage vortex, a spanwise domain size of $L_z = 0.5C$ seems to be adequate in the case of a moving end wall.

The corresponding Reynolds stresses also appear reasonable relative to experimental measurements. As seen in Figs. 16 and 17, the tip-leakage vortex is the main source of turbulence generation in the downstream flowfield and results in low-pressure fluctuations near the end-wall region. The discrepancy between the computed and experimental turbulence intensity levels is most likely caused by the sampling time over which statistics are accumulated. Obtaining adequate statistical samples for these fully inhomogeneous flows remains a challenge for these computer-intensive simulations.

Figure 18 shows the instantaneous and time-averaged pressure contours in an x–y plane very close to the moving endwall ($z = 0.008C_a$). The spatial variations of the negative pressure relative to the mean values appear to be highly correlated with the tip-leakage flow. These results indicate that a strong circular motion is developed by the tip-leakage vortex around the low-pressure core and this structure travels downstream expanding in size and generating intense fluctuations in the endwall region.

The energy spectra from the present LES and the experiment[11] in the tip-leakage region ($x = 1.51C_a$, $y = 1.4C_a$, $z = 0.1C_a$) are shown in Fig. 19. The spectra from both the LES and the experiment clearly show the presence of the inertial subrange. The spectral peaks suggest the presence of distinct coherent motions in the tip-leakage flow. The present numerical scheme appears to be good in predicting the energies in a wide frequency range without excessive numerical dissipation.

IV. Summary

To analyze the temporal and spatial dynamics of the rotor-tip-clearance flow and determine the underlying mechanism for the low-pressure fluctuations, a large-eddy simulation code that combines an immersed-boundary technique with a generalized curvilinear structured grid has been developed. Key numerical aspects including the implementation of immersed boundary method, the SGS model for fully inhomogeneous flow, and grid skewness have been examined. Results from the simulations show that the method is capable of capturing the complex flow features observed in well-documented experiments. The flowfield is found to exhibit strong circular motions associated with the tip-leakage and tip-separation vortices. These vortical structures are found to convect downstream, expand in size, and generate intense turbulent fluctuations in the endwall region. Qualitative and quantitative agreements with experiments in terms of velocity, Reynolds stresses, and energy spectra have been observed in the downstream measurement locations. A detailed analysis of the data generated from these simulations should allow us to gain some insight into the spatiotemporal dynamics of the tip-clearance flow and mechanisms for cavitation-inducing low-pressure fluctuations. Results from this analysis will be presented in the future.

Acknowledgments

The authors acknowledge the support of the Office of Naval Research under Grant N00014-99-1-0389, with Ki-Han Kim and Patrick Purtell as Program Managers. Computer time was provided by a U.S. Department of Defense Challenge Project Grant (C82) through the Army Research Laboratory and Aeronautical Systems Center Major Shared Resource Centers. The authors also thank William Devenport of Virginia Polytechnic Institute and State University for providing his experimental data. A preliminary version of this work was presented as Paper 2003-45395 at the 2003 Joint American Society of Mechanical Engineers/Japan Society of Mechanical Engineers Fluids Engineering Summer Conference, Honolulu, Hawaii, 6–10 June 2003.

References

[1]Hoeger, M., Fritsch, G., and Bauer, D.,"Numerical Simulation of the Shock-Tip Leakage Vortex Interaction in a HPC Front Stage," *Journal of Turbomachinery*, Vol. 121, 1999, pp. 456–468.

[2]Ameri, A. A., Steinthorsson, E., and Rigby, D. L., "Effects of Tip Clearance and Casing Recess on Heat Transfer and Stage Efficiency in Axial Turbines," *Journal of Turbomachinery*, Vol. 121, 1999, pp. 683–693.

[3]Wenger, C. W., Devenport, W. J., Wittmer, K. S., and Muthanna, C., "Two-Point Measurements in the Wake of a Compressor Cascade," AIAA Paper 98-2556, June 1998.

[4]Kameier, F., and Neise, W., "Experimental Study of Tip Clearance Losses and Noise in Axial Turbomachines and Their Reduction," *Journal of Turbomachinery*, Vol. 119, 1997, pp. 460–471.

[5]Zierke, W. C., Farrel, K. J., and Straka, W. A., "Measurement of the Tip Clearance Flow for a High-Reynolds-Number Axial-Flow Rotor," *Journal of Turbomachinery*, Vol. 119, 1995, pp. 1–8.

[6]Kang, S., and Hirsch, C., "Experimental Study on the Three-Dimensional Flow within a Compressor Cascade with Tip Clearance: Part I—Velocity and Pressure Fields, and Part II—The Tip Leakage Vortex," *Journal of Turbomachinery*, Vol. 115, 1993, pp. 435–443.

[7]Kang, S., and Hirsch, C., "Tip Leakage Flow in Linear Compressor Cascade," *Journal of Turbomachinery*, Vol. 116, 1994, pp. 657–664.

[8]Storer, J. A., and Cumpsty, N. A., "Tip Leakage Flows in Axial Compressors," American Society of Mechanical Engineers, Paper 90-GT-127, June 1990.

[9]Muthanna, C., "Flowfield Downstream of a Compressor Cascade with Tip Leakage," M.S. Thesis, Dept. of Aerospace and Ocean Engineering, Virginia Polytechnic Inst. and State Univ., Blacksburg, VA, Nov. 1998.

[10]Muthanna, C., "The Effects of Free Stream Turbulence on the Flow Field through a Compressor Cascade," Ph.D. Dissertation, Dept. of Aerospace and Ocean Engineering, Virginia Polytechnic Inst. and State Univ., Blacksburg, VA, May 2002.

[11]Wang, Y., "Tip Leakage Flow Downstream of a Compressor Cascade with Moving End Wall," M.S. Thesis, Dept. of Aerospace and Ocean Engineering, Virginia Polytechnic Inst. and State Univ., Blacksburg, VA, Feb. 2000.

[12]Kuhl, D. D., "Near Wall Investigation of Three Dimensional Turbulent Boundary Layers," M.S. Thesis, Dept. of Aerospace and Ocean Engineering, Virginia Polytechnic Inst. and State Univ., Blacksburg, VA, Aug. 2001.

[13]Khorrami, M. R., Li, F., and Choudhan, M., "Novel Approach for Reducing Rotor Tip-Clearance-Induced Noise in Turbofan Engines," *AIAA Journal*, Vol. 40, No. 8, 2002, pp. 1518–1528.

[14]Shin, S., "Reynolds-Averaged Navier–Stokes Computation of Tip-Clearance Flow in a Compressor Cascade Using an Unstructured Grid," Ph.D. Dissertation, Dept. of Aerospace Engineering, Virginia Polytechnic Inst. and State Univ., Blacksburg, VA, Sept. 2001.

[15]Kunz, R. F., Lakshminarayana, B., and Basson, A. H., "Investigation of Tip Clearance Phenomena in an Axial Compressor Cascade Using Euler and Navier–Stokes Procedures," *Journal of Turbomachinery*, Vol. 115, 1993, pp. 453–467.

[16]Choi, H., Moin, P., and Kim, J., "Turbulent Drag Reduction: Studies of Feedback Control and Flow over Riblets," Dept. of Mechanical Engineering, Stanford Univ., Rept. TF-55, Stanford, CA, Sept. 1992.

[17]Beaudan, P., and Moin, P., "Numerical Experiments on the Flow past a Circular Cylinder at Sub-Critical Reynolds Number," Dept. of Mechanical Engineering, Stanford Univ., Rept. TF-62, Stanford, CA, Dec. 1994.

[18]Mittal, R., and Moin, P., "Suitability of Upwind-Biased Schemes for Large-Eddy Simulation of Turbulent Flows," *AIAA Journal*, Vol. 36, 1997, pp. 1415–1417.

[19]Meneveau, C., Lund, T. S., and Cabot, W. H., "A Lagrangian Dynamic Subgrid-Scale Model of Turbulence," *Journal of Fluid Mechanics*, Vol. 319, 1996, pp. 233–242.

[20]Germano, M., Piomelli, U., Moin, P., and Cabot, W. H., "A Dynamic Subgrid-Scale Eddy-Viscosity Model," *Physics of Fluids A*, Vol. 3, 1991, pp. 1760–1765.

[21]Lund, T. S., Wu, X., and Squires, K. D., "Generation of Turbulent Inflow Data for Spatially-Developing Boundary Layer Simulations," *Journal of Computational Physics*, Vol. 140, 1998, pp. 233–258.

[22]You, D., Mittal, R., Wang, M., and Moin, P., "Large-Eddy Simulation of a Rotor Tip-Clearance Flow," AIAA Paper 2002-0981, Jan. 2002.

[23]Thompson, J. F., Warsi, Z. U. A., and Mastin, C. W., *Numerical Grid Generation: Foundation and Applications*, North-Holland, New York, 1985, pp. 171–184.

[24]Fadlun, E. A., Verzicco, R., Orlandi, P., and Mohd-Yusof, J., "Combined Immersed-Boundary Finite-Difference Methods for Three-Dimensional Complex Flow Simulations," *Journal of Computational Physics*, Vol. 161, 2000, pp. 35–60.

[25]Park, J., Kwon, K., and Choi, H., "Numerical Solutions of Flow Past a Circular Cylinder at Reynolds Numbers up to 160," *Korean Society of Mechanical Engineers International Journal*, Vol. 12, 1998, pp. 1200–1205.

[26]Williamson, C. H. K., "Oblique and Parallel Modes of Vortex Shedding in the Wake of a Circular Cylinder at Low Reynolds Numbers," *Journal of Fluid Mechanics*, Vol. 206, 1989, pp. 579–627.

[27]Mittal, R., Venkatasubramanian, S., and Najjar, F. M., "Large Eddy Simulation of Flow Through a Low-Pressure Turbine," AIAA Paper 2001-2560, June 2001.

[28]Gresho, P. M., and Lee, R. L., "Don't Suppress Wiggles—They're Telling You Something," *Computers and Fluids*, Vol. 9, 1981, pp. 223–253.

[29]Jeong, J., and Hussain, F., "On the Identification of a Vortex," *Journal of Fluid Mechanics*, Vol. 285, 1995, pp. 69–94.

P. Givi
Associate Editor